



Measurement of competitive CO₂ and N₂ adsorption on Zeolite 13X for post-combustion CO₂ capture

Nicholas Stiles Wilkins¹ · Arvind Rajendran¹

Received: 28 October 2018 / Revised: 21 December 2018 / Accepted: 22 December 2018 / Published online: 6 January 2019
© Springer Science+Business Media, LLC, part of Springer Nature 2019

Abstract

Single component CO₂ and N₂ equilibrium loadings were measured on Zeochem Zeolite 13X from 0 to 150 °C and 0–5 bar using volumetry and gravimetry. CO₂ equilibrium data was fit to a dual-site Langmuir (DSL) isotherm. The equilibrium data for N₂ was fit using four isotherm schemes: two single site Langmuir isotherms, the DSL with the equal energy sites and the DSL with unequal energy site pairings. A series of single and multicomponent CO₂ and N₂ dynamic column breakthrough (DCB) experiments were measured on Zeolite 13X at 22 °C and 0.98 bar. The adsorption breakthrough experiments were able to provide accurate data for CO₂ competitive adsorption, while failing to provide reliable N₂ data. It was shown that desorption experiments from a bed fully saturated with the desired composition provides a better estimate of the competitive N₂ loading. A detailed mathematical model that used inputs from the batch equilibrium experiments was able to predict the composition and thermal breakthrough curves well while underpredicting the single component N₂ loading. The DSL isotherm with unequal energy sites was shown to predict the competitive loading and breakthrough curves well. The impact of the chosen adsorption isotherm model on process performance was evaluated by simulating a 4-step vacuum swing adsorption process to concentrate CO₂ from dry post-combustion flue gas. The results show that the purity, recovery, energy and productivity are affected by the choice of the competitive adsorption isotherm.

Keywords Dynamic column breakthrough · Desorption · Post-combustion carbon capture · Carbon dioxide · Nitrogen · Zeolite 13X

Abbreviations

CCS	Carbon capture and storage
DCB	Dynamic column breakthrough
DSL	Dual-site Langmuir isotherm
DOE	Department of energy
EES	Equal energy site DSL model
IAST	Ideal adsorbed solution theory
LDF	Linear driving force
MFC	Mass flow controller
MFM	Mass flow meter
MS	Mass spectrometer

MSB	Magnetic suspension balance
ODE	Ordinary differential equation
PN	Perfect negative pairing
PP	Perfect positive pairing
PSA	Pressure-swing adsorption
PT	Pressure transducer
Δ PT	Differential pressure transducer
SSL	Single-site Langmuir model
TC	Thermocouple
UES	Unequal energy site DSL model
VSA	Vacuum-swing adsorption

Roman symbols

<i>A</i>	Adsorbent surface area (m ²)
<i>b</i>	Adsorption equilibrium constant for site 1 (m ³ mol ⁻¹)
<i>c</i>	Fluid phase concentration (mol m ⁻³)
<i>C_p</i>	Heat capacity (J mol ⁻¹ K ⁻¹)
<i>d</i>	Adsorption equilibrium constant for site 2 (m ³ mol ⁻¹)
<i>D</i>	Diffusivity (m ² s ⁻¹)

Electronic supplementary material The online version of this article (<https://doi.org/10.1007/s10450-018-00004-2>) contains supplementary material, which is available to authorized users.

✉ Arvind Rajendran
arvind.rajendran@ualberta.ca

¹ Department of Chemical and Materials Engineering, University of Alberta Donadeo Innovation Centre of Engineering, 9211-116 Street NW, Edmonton, AB T6G 1H9, Canada

E	Energy consumption (kWh _e tonne of CO ₂ captured ⁻¹)
h	Heat transfer coefficient (W m ⁻² K ⁻¹)
ΔH	Heat of adsorption (J mol ⁻¹)
k	Mass transfer coefficient (s ⁻¹)
K	Thermal conductivity (W m ⁻¹ K ⁻¹)
L	Length (m)
m	Adsorbent mass (kg)
n	Number of species (–)
p	Partial pressure (bar)
P	Total pressure (bar)
Pu	Purity (mol%)
Pr	Productivity (mol CO ₂ m ⁻³ s ⁻¹)
q	Solid phase loading (mol kg ⁻¹)
q^*	Equilibrium solid phase loading (mol kg ⁻¹)
Q	Outlet volumetric flow rate (m ³ s ⁻¹)
r	Radius (m)
R	Universal gas constant (Pa m ³ mol ⁻¹ K ⁻¹)
Re	Recovery (%)
t	Time (s)
\bar{t}	dimensionless time (–)
T	Temperature (K)
ΔU	Internal energy (J mol ⁻¹)
v	Interstitial velocity (m s ⁻¹)
V	Volume (m ³)
x	Solid phase fraction (–)
y	Mole fraction (–)
z	Axial direction (m)

Greek symbols

α	Competitive selectivity (–)
γ	C_p/C_v (–)
ϵ	Bed voidage (–)
η	Vacuum pump efficiency (–)
μ	Viscosity (Pa s ⁻¹)
π	Spreading pressure (Pa)
ρ	Adsorbent density (kg m ⁻³)
τ	Tortuosity (–)

Subscripts and superscripts

a	Adsorbed phase
acc	Solid and fluid phase accumulation
ads	Adsorbent or adsorption
amb	Ambient
ADS	Adsorption step
ave	Average
b	Bed or column
BLO	Blowdown step
comp	Component
d	Extra-column
des	Desorption
EVAC	Evacuation step
g	Fluid phase
H	High

i	Index of species
I	Intermediate
iso	Isosteric
in	Inlet or internal
L	Length or low
LPP	Light product pressurization
m	Molecular
o	At the spreading pressure
out	Outlet or external
p	Particle
scaled	Linear regression fit energy
s	Solid phase
sat	Ultimate saturation
tot	Total
w	Wall
z	Axial direction
0	Initial

1 Introduction

Anthropogenic CO₂ emissions are driving climate change (Stern 2008). One proposed solution to mitigate CO₂ emissions is carbon capture and storage (CCS) from point sources such as power plants. CCS is the process of capturing and concentrating CO₂, before the flue gas is released to the environment, and storing it underground. One method to capture CO₂ is through post-combustion carbon capture, or capturing the CO₂ after the fuel is burned for power (Samanta et al. 2011; Bui et al. 2018). Although liquid absorption is the current method of choice for the CO₂ capture step, it suffers from high parasitic energy requirements and solvent degradation (IPCC 2005). Adsorption using solid adsorbents has been suggested as a possible alternative to capture CO₂ from the effluent gas stream (Zanco et al. 2017). In a traditional power plant, fuel and air are fed to a furnace and combusted to yield primarily H₂O and CO₂. The N₂ and excess O₂ from air remains unreacted. On a dry basis, after the desulphurization step, the flue gas is a mixture of ≈ 12 – 15 mol% CO₂ and the rest being N₂ and O₂ (Samanta et al. 2011).

Many adsorbents are being studied for their potential use in CO₂ capture from large point sources (Smit et al. 2014; Boot-Handford et al. 2014). Among them, Zeolite 13X is considered the benchmark adsorbent for post-combustion carbon capture, not only due to its large selectivity of CO₂ over N₂, but also because it is cheap and currently used in other commercial separations. Many process-scale studies point to the fact that Zeolite 13X is capable of reaching the U.S. Department of Energy (US-DOE) targets for CO₂ purity and recovery (Haghpanah et al. 2013a; Krishnamurthy et al. 2014a). Further, the efficacy of Zeolite 13X for the separation of CO₂ and N₂ at post-combustion conditions has been demonstrated at pilot plant scales (Krishnamurthy

et al. 2014a; Lu et al. 2012; Xiao et al. 2008). Krishnamurthy et al. reported cycles that achieved high purity ($\approx 95\%$) and high recovery ($\approx 90\%$) from a feed containing 15 mol% CO_2 (Krishnamurthy et al. 2014a). The separation mechanism of CO_2 and N_2 on Zeolite 13X is based on differences in the equilibrium adsorption of these gases. Therefore, it is critical to obtain the adsorption isotherms for the adsorbent. CO_2 and N_2 adsorption on Zeolite 13X is well studied. Several reports exist and data can be easily obtained from public databases (Hocker et al. 2003; Cavenati et al. 2006; Wang and LeVan 2009; Krishnamurthy et al. 2014a; Hefti et al. 2015). In some of the recent literature, specifically those dealing with metal–organic frameworks (MOFs), it is increasingly common only to see only reports of CO_2 adsorption, while ignoring measurement of N_2 adsorption. Recent studies have pointed out that measuring N_2 isotherms on the same sample is critical for reliable process simulations (Rajagopalan et al. 2016; Rajagopalan and Rajendran 2018; Farmahini et al. 2018).

Understanding and quantifying competitive adsorption is critical for process design (Sircar 2006). However, it is surprising to note the lack of experimental studies that report the competitive adsorption of CO_2 and N_2 on such a common material as Zeolite 13X (Hefti et al. 2015; Purdue 2018; Avijegon et al. 2018). The lack of competitive data at low pressures (< 1 bar), i.e., conditions at which most processes for post-combustion CO_2 capture are optimal, is glaring. Most process modeling studies have been performed with the assumption that single component isotherms can be used either with the ideal adsorbed solution theory or the competition can be described by simple extensions of the single component models (Xiao et al. 2008; Krishnamurthy et al. 2014b). Further, the impact of such assumptions on predicting process performance is not well studied. These outstanding issues provide the motivation for the current work where the main aim is to measure low pressure isotherms of CO_2 and N_2 on the same Zeolite 13X sample, quantify the competition by measuring competitive loadings and proposing an explicit competitive isotherm validated with dynamic column breakthrough (DCB) experiments and to demonstrate the importance of proper characterization of competitive adsorption on process performance.

As previously mentioned only a few papers have studied the competition of CO_2 and N_2 on the same sample of Zeolite 13X (Hefti et al. 2015; Purdue 2018; Avijegon et al. 2018). Hefti et al. studied single and multicomponent CO_2 and N_2 mixtures on Zeolite 13X at 1.2, 3.0 and 10.0 bar total pressures at 25 °C and 45 °C using a magnetic suspension balance (MSB) (Hefti et al. 2015). The CO_2/N_2 mixtures in Hefti et al. are primarily at relatively high N_2 and low CO_2 concentrations to study the non-ideality of the mixture on Zeolite 13X (Hefti et al. 2015). Hefti et al. found the extended Sips equilibrium model fit the competitive data

reasonably although under-predicting the competition (Hefti et al. 2015). Purdue used the experimentally collected competitive CO_2/N_2 equilibrium data from Hefti et al. to study the competition of CO_2 , N_2 and H_2O on Zeolite 13X using grand-canonical Monte Carlo (GCMC) simulations (Purdue 2018). Purdue was able to confirm the data that was collected by Hefti et al. at 25 °C and predicted the CO_2/N_2 competitive loadings at 50 °C and 70 °C (Purdue 2018). Avijegon et al. measured competitive loadings of CO_2 , N_2 and CH_4 mixtures on Zeolite 13X using DCB experiments (Avijegon et al. 2018). Avijegon et al. measured multicomponent loadings by sending a step input of adsorbing gas into an activated Zeolite 13X bed and solving the transient mass balance (Avijegon et al. 2018). The authors were able to easily measure the CO_2 competitive loadings, but were not able to measure the N_2 loadings with certainty, particularly at low N_2 concentrations in their binary CO_2/N_2 mixtures; the experimental uncertainty was larger than the calculated N_2 loadings (Avijegon et al. 2018). This clearly highlighted the challenges of measuring the loading of the lighter component in a binary mixture, especially in a case where competition is very strong.

In this paper, the single component isotherms of CO_2 and N_2 are measured using two techniques: volumetry and gravimetry. The competition between CO_2 and N_2 is studied through DCB adsorption and desorption experiments. Single and multicomponent equilibrium data for N_2 and CO_2 are reported for temperatures and pressures around post-combustion process conditions on Zeolite 13X. These experiments were described with a detailed model and a suitable competitive isotherm that describes both the competitive loadings and the DCB profiles. Some key challenges faced during the measurement of strongly competitive species are elaborated and ways to overcome those challenges are discussed. Finally, the importance of competitive behaviour is illustrated using process studies. Specifically, the choice of a competitive equilibrium description and its effect on the predictions of process performance.

2 Materials and methods

Zeolite 13X (Z10-02ND) was obtained from Zeochem (Uetikon am See, Switzerland). This particular Zeolite 13X has a stronger affinity and higher CO_2 loading compared to another material that has been reported by Krishnamurthy et al. (2014a) but, it is similar to the one that was studied by Hefti et al. (2015). The Zeolite 13X particles are spherical and have a diameter between 0.8 and 1.2 mm. The Langmuir and BET surface areas, and the internal pore volume of Zeolite 13X were measured with a volumetric liquid N_2 isotherm at -196 °C using a Micromeritics ASAP 2020 (Norcross, GA, USA). The Langmuir and BET surface areas

were measured to be $859 \pm 2 \text{ m}^2 \text{ g}^{-1}$ and $575 \pm 21 \text{ m}^2 \text{ g}^{-1}$, respectively. The internal pore volume was determined to be $2.995 \times 10^{-7} \text{ m}^3 \text{ g}^{-1}$. All gases in this study (99.999% He, 99.998% CO_2 , 99.999% N_2) were obtained from Praxair Canada.

Single component adsorption isotherms for CO_2 and N_2 were measured using volumetry and gravimetry. Single and multicomponent adsorption equilibrium and column dynamics were measured with DCB adsorption and desorption experiments. In all cases, the focus was on measurements at low pressures ($< 1 \text{ bar}$). At these conditions, the fluid phase density is significantly lower than the adsorbed phase density; therefore the measured loadings can be treated as the absolute amount adsorbed (Sircar 1999; Hocker et al. 2003)

2.1 Volumetry

Volumetric isotherms for CO_2 and N_2 were measured with a Micromeritics ASAP 2020 (Norcross, GA, USA). The Micromeritics system can measure adsorption equilibrium between 1 mbar up to 1.2 bar. Volumetric equilibrium data is measured by dosing an initially evacuated chamber, filled with some adsorbent, with known volumes of gas. The resulting change in pressure is proportional to the amount of gas adsorbed. Prior to each volumetric isotherm experiment, the sample was regenerated for 12 h under vacuum at $350 \text{ }^\circ\text{C}$. The volumetric system has an loading accuracy of $< 0.15\%$ of the reading and pressure accuracy of $< 1.3 \times 10^{-7} \text{ mbar}$. A sample mass of $\approx 200 \text{ mg}$ was used for these experiments.

2.2 Gravimetry

Gravimetric isotherms for CO_2 and N_2 were measured with a Rubotherm Type E10 (Bochum, Germany) MSB. The MSB can measure from 0.2 bar up to 50 bar. The gravimetric equilibrium loading is measured by placing $\approx 2 \text{ g}$ of adsorbent on the MSB and measuring the mass change as a function of the pressure (Hocker et al. 2003). Prior to each gravimetric isotherm experiment, the sample was regenerated under vacuum at $350 \text{ }^\circ\text{C}$ for 12 h. Before the CO_2 and N_2 isotherm measurements, experiments using He were performed to measure the skeletal volume of the adsorbent. Helium was assumed to be non-adsorbing. This assumption is reasonable since only low pressure data ($< 5 \text{ bar}$) was targeted (Rajendran et al. 2002).

2.3 Dynamic column breakthrough experiments

The DCB apparatus used in this study is shown in Fig. 1. The mass flow controllers control the flow of the gasses. Controllers for “gas 1” and “gas 2” were purchased from Parker/Porter (Hatfield, PA, USA) with a maximum flowrate

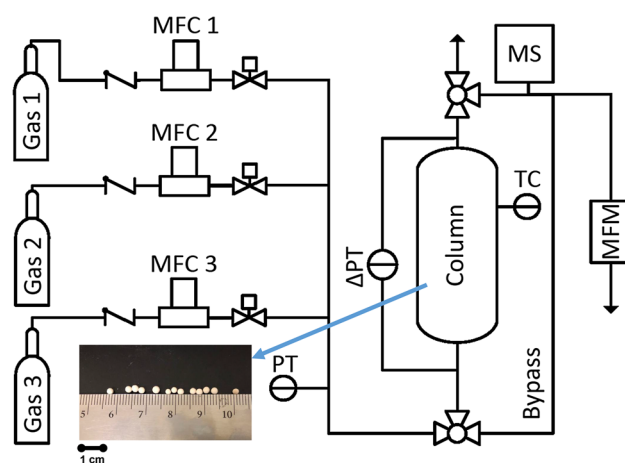


Fig. 1 Schematic of the DCB apparatus. *MFC* mass flow controller, *MFM* mass flow meter, *MS* mass spectrometer, *PT* pressure transducer, ΔPT differential pressure transducer, *TC* thermocouple. The Z10-02ND Zeolite 13X sample is also shown with a ruler for scale

of 5 SLPM, while the controller for “gas 3” was purchased from Alicat Scientific (Tucson, AZ, USA) and can control the flow up to 500 sccm. The outlet mass flow meter (Parker/Porter, Hatfield, PA) can measure up to 1 SLPM. The heart of the system is a stainless steel column (Swagelok 304L-HDF2-40) with a packed length of 6.4 cm and a diameter of 2.82 cm containing 23.02 g of adsorbent. One thermocouple (Omega Engineering, Laval, QC, Canada) was kept 5.2 cm from the column inlet. The inlet pressure and pressure drop were measured using a pressure transducer and differential pressure gauge, respectively (GE Druck, Billerica, MA, USA). The gas composition at the column outlet was measured with a mass spectrometer (Pfeiffer Vacuum OmniStar GSD 320, Asslar, Germany) that was calibrated before each experiment with known gas compositions. All necessary quantities were recorded in a data acquisition system built using LabView. The temperature in the lab was maintained at $\approx 22 \text{ }^\circ\text{C}$. Before each breakthrough experiment, the column was regenerated at $350 \text{ }^\circ\text{C}$ under 350 sccm of helium for 12 h. All breakthrough experiments were performed at $\approx 22 \text{ }^\circ\text{C}$ and $\approx 0.97 \text{ bar}$ total pressure. Since the extra-column volume of the DCB apparatus was 0.6 mL (which is 1.5% of the column volume), no correction procedures were used to treat the breakthrough profiles (Rajendran et al. 2008). Blank experiments show that the average spread (from 5 to 95% signal of the step response) in the dead volume was small $\bar{i} \approx 0.3$, which is negligible compared to the spread of the adsorption and desorption experiments.

For an adsorption breakthrough experiment, at time $t < 0$ a carrier gas flowed through the column. At $t = 0$, a step signal of pure or mixed gas was sent through the column. The outlet compositions, inlet and outlet flows, pressure, pressure

drop and temperature were recorded in a data acquisition system. This step signal continues for some time until the compositions and thermal breakthroughs were completed. For a desorption experiment, at time $t < 0$ a single or multicomponent adsorbing gas flows through the column until the column is saturated with the feed. At $t = 0$, a step signal of inert gas is sent through the column. The pressure drop in the system was < 0.02 bar and is therefore considered negligible.

Prior to each experiment, flow and composition calibrations were performed. The effluent composition detected in the MS was calibrated using gas cylinders of known compositions. The effluent mass flow meter was calibrated first using pure CO_2 , N_2 and He by setting an inlet flow on one of the mass flow controllers, and measuring the real outlet flow and the mass flow meter signal. Then, different mixtures of CO_2 , N_2 and He were made at different flowrates to build a calibration curve of real flow as a function of the effluent compositions and the mass flow meter signal.

3 Modeling

3.1 Dynamic column breakthrough simulation

The adsorption dynamics of the column were modeled based on the following assumptions:

1. The gas phase is ideal. The experiments were all performed at low pressures so the ideal gas assumption is justified.
2. The column is one-dimensional and there are no radial gradients for concentration or temperature.
3. An axially dispersed plug flow model adequately describes the flow through the column.
4. The ambient temperature is uniform. This was confirmed by measurements in the laboratory. The variation over a single experiment was < 0.5 °C.
5. Darcy’s law adequately describes the pressure drop in the column. The flowrates were low and the measured pressure drop was small (< 0.02 bar).
6. The solid and gas phases achieve thermal equilibrium instantaneously.
7. The adsorbent and bed properties are uniform throughout the column.
8. The linear driving force (LDF) model adequately describes the solid phase mass transfer rate. The LDF coefficient was calculated from the expression for molecular diffusion in the macropores. This mechanism has been demonstrated to be the controlling mechanism for CO_2 in Zeolite 13X (Hu et al. 2014).

With these assumptions, the gas phase mass balance, which accounts for dispersive, convective and adsorptive effects within the column, is given by:

$$\frac{\partial c_i}{\partial t} = \frac{\partial}{\partial z} \left(cD_L \frac{\partial y_i}{\partial z} + c_i v \right) - \frac{1 - \epsilon}{\epsilon} \frac{\partial q_i}{\partial t} \tag{1}$$

For the independent variables, z is the axial length and t is the time. For the dependent variables, c is the total gas phase concentration, while c_i , y_i and q_i are the fluid phase concentration, the fluid phase mole fraction and the solid phase loading of component i , v is the interstitial velocity, ϵ is the bed void fraction and D_L is the axial dispersion coefficient. If the ideal gas law is assumed, c in Eq. 1 can be expanded. For an ideal gas, using $c = P/RT$, where P is the pressure, R is the universal gas constant and T is the temperature, the component mass balance can be written as:

$$\begin{aligned} \frac{\partial y_i}{\partial t} + \frac{y_i}{P} \frac{\partial P}{\partial t} - \frac{y_i}{T} \frac{\partial T}{\partial t} = D_L \frac{T}{P} \frac{\partial}{\partial z} \left(\frac{P}{T} \frac{\partial y_i}{\partial z} \right) \\ - \frac{T}{P} \frac{\partial}{\partial z} \left(\frac{y_i P}{T} v \right) - \frac{RT}{P} \frac{1 - \epsilon}{\epsilon} \frac{\partial q_i}{\partial t} \end{aligned} \tag{2}$$

If all component mass balances are summed, the overall mass balance can be written as:

$$\frac{1}{P} \frac{\partial P}{\partial t} - \frac{1}{T} \frac{\partial T}{\partial t} = - \frac{T}{P} \frac{\partial}{\partial z} \left(\frac{P}{T} v \right) - \frac{RT}{P} \frac{1 - \epsilon}{\epsilon} \sum_{i=1}^{n_{\text{comp}}} \frac{\partial q_i}{\partial t} \tag{3}$$

Mass transfer in the solid phase is described by the linear driving force model:

$$\frac{\partial q_i}{\partial t} = k_i (q_i^* - q_i) \tag{4}$$

where q^* is the equilibrium loading and k_i is LDF coefficient. The equilibrium loading, q^* can be represented by a suitable adsorption isotherm

$$q^* = q^*(y, P, T) \tag{5}$$

The LDF coefficient is a lumped parameter which, for the case of a system that is controlled by molecular diffusion in the macropores, is described as:

$$k_i = \frac{15 \epsilon_p D_p}{r_p^2} \frac{c_i}{q_i^*} \tag{6}$$

where ϵ_p is the particle void fraction, r_p is the particle radius and D_p is the macropore diffusivity, which is a function of molecular diffusion, D_m (calculated from the Chapman–Enskog equation) and the adsorbent tortuosity, τ (Ruthven 1984; Gleuckauf and Coates 1947).

$$D_p = \frac{D_m}{\tau} \tag{7}$$

Darcy's law describes the axial pressure drop across the column:

$$-\frac{\partial P}{\partial z} = \frac{150}{4} \frac{1}{r_p^2} \left(\frac{1-\epsilon}{\epsilon} \right)^2 \mu v \quad (8)$$

where μ is the gas phase viscosity, which is assumed to be constant during the process. The column energy balance includes thermal effects due to conduction through the column wall, convection along the bed and adsorption:

$$\begin{aligned} \left[\frac{1-\epsilon}{\epsilon} (\rho_s C_{p,s} + C_{p,a} \sum_{i=1}^{n_{\text{comp}}} q_i) \right] \frac{\partial T}{\partial t} &= \frac{K_z}{\epsilon} \frac{\partial^2 T}{\partial z^2} - \frac{C_{p,g}}{R} \frac{\partial}{\partial z} (vP) \\ &- \frac{C_{p,g}}{R} \frac{\partial P}{\partial t} - \frac{1-\epsilon}{\epsilon} C_{p,a} T \sum_{i=1}^{n_{\text{comp}}} \frac{\partial q_i}{\partial t} + \frac{1-\epsilon}{\epsilon} \sum_{i=1}^{n_{\text{comp}}} \left[(-\Delta H_i) \frac{\partial q_i}{\partial t} \right] \\ &- \frac{2h_{\text{in}}}{\epsilon r_{\text{in}}} (T - T_w) \end{aligned} \quad (9)$$

where ρ_s is the particle density, $C_{p,s}$ is the solid heat capacity, $C_{p,g}$ is the fluid heat capacity, $C_{p,a}$ is the adsorbed phase heat capacity, K_z is the thermal conductivity of the gas, ΔH_i is the heat of adsorption of component i , h_{in} is the internal heat transfer coefficient, r_{in} is the internal radius of the column and T_w is the column wall temperature. The energy balance on the column wall is written as:

$$\rho_w C_{p,w} \frac{\partial T_w}{\partial t} = K_w \frac{\partial^2 T_w}{\partial z^2} + \frac{2r_{\text{in}} h_{\text{in}}}{r_{\text{out}}^2 - r_{\text{in}}^2} (T - T_w) - \frac{2r_{\text{out}} h_{\text{out}}}{r_{\text{out}}^2 - r_{\text{in}}^2} (T_w - T_{\text{amb}}) \quad (10)$$

where ρ_w is the density of the column wall, $C_{p,w}$ is the heat capacity of the column wall, K_w is the thermal conductivity of the column wall, r_{out} is the external radius of the column, h_{out} is the external heat transfer coefficient and T_{amb} is the ambient temperature outside of the column.

The axial dispersion coefficient, D_L , is a lumped parameter that is a combination of the molecular diffusion, D_m , and turbulent mixing which can be written as (Ruthven 1984).

$$D_L = 0.7D_m + vr_p \quad (11)$$

The model equations were discretized in the axial direction using a finite volume scheme employing a WENO flux limiter. The column was discretized into 30 finite volumes. The resulting set of ordinary differential equations (ODE) were solved using *ode15s*, an explicit inbuilt MATLAB ODE solver. The details are explained in earlier publications (Haghpahan et al. 2013a; Hosseinzadeh Hejazi et al. 2016).

3.2 Mass balance calculations

Since there is no reaction within the column, the following molar balance can be written for the case of an adsorption experiment (Guntuka et al. 2008).

$$n_{\text{acc}} = n_{\text{in}} - n_{\text{out}} \quad (12)$$

The accumulation, n_{acc} , is the difference between the moles entering the column, n_{in} , and the moles leaving the column, n_{out} . Part of the accumulation is in the solid phase and the remaining amount is in the fluid. Assuming that the ideal gas law is valid, at the end of a DCB experiment the individual terms can be written as:

$$\begin{aligned} m_{\text{ads}} q_i^* + \frac{y_{i,\text{in}} P_{\text{avg}}}{RT_{\text{in}}} (V_b \epsilon + V_d) &= \int_0^{t_{\text{ads}}} \left(\frac{y_{i,\text{in}} P_{\text{ave}} Q_{\text{in}}}{RT_{\text{in}}} \right) dt \\ &- \int_0^{t_{\text{ads}}} \left(\frac{y_{i,\text{out}} P_{\text{ave}} Q_{\text{out}}}{RT_{\text{out}}} \right) dt \end{aligned} \quad (13)$$

In Eq. 13, Q is the actual gas volumetric flowrate, V_b is the total bed volume, V_d is the extra-column volume, sometimes called the dead volume, and q_i^* is the averaged equilibrium loading. Solving Eq. 13 for q_i^* yields the equilibrium loading for the adsorbent for the particular set of conditions (Guntuka et al. 2008). In all experiments performed, the pressure drop across the column was negligible (< 0.02 bar), therefore the average column pressure was used, $P_{\text{ave}} = \frac{P_{\text{in}} + P_{\text{out}}}{2} \approx P$. Note that Eq. 13 can be used to measure the competitive loadings in multicomponent mixtures provided that independent equations are written for each of the components in the experiment. The measured q_i^* provides the loading corresponding to the partial pressures of each species, $y_{i,\text{in}} P_{\text{ave}}$ and temperature, T . Note that it is important for the experiment to proceed as long as its required for both the compositions and thermal breakthrough to occur.

For the case of a desorption experiment with an inert feed, the mass balance can be written as:

$$n_{\text{acc}} = n_{\text{out}} \quad (14)$$

Again, assuming that the ideal gas law is valid, at the end of a desorption experiment the individual terms can be written as:

$$m_{\text{ads}} q_i^* + \frac{y_{i,\text{in}} P_{\text{avg}}}{RT_{\text{in}}} (V_b \epsilon + V_d) = \int_0^{t_{\text{des}}} \left(\frac{y_{i,\text{out}} P_{\text{ave}} Q_{\text{out}}}{RT_{\text{out}}} \right) dt \quad (15)$$

where q_i^* is the solid phase loading at $t = 0$. In this situation it is important to wait until the column is both saturated with the desired feed and thermally equilibrated before flow is switched to the sweep gas. Also, it is important to perform these experiments where the ΔP across the column is low to satisfy the condition that q_i^* is uniform across the column.

The fluid and solid accumulation of a given component can be determined graphically from the addition or subtraction of shaded areas in Fig. 2. For a single component system, let us just consider component 2 in Fig. 2. For adsorption, the accumulation is area **C**; for desorption, the accumulation is area **E**. For a hypothetical mixture of component 1 and 2 (both components are normalized with their component feed

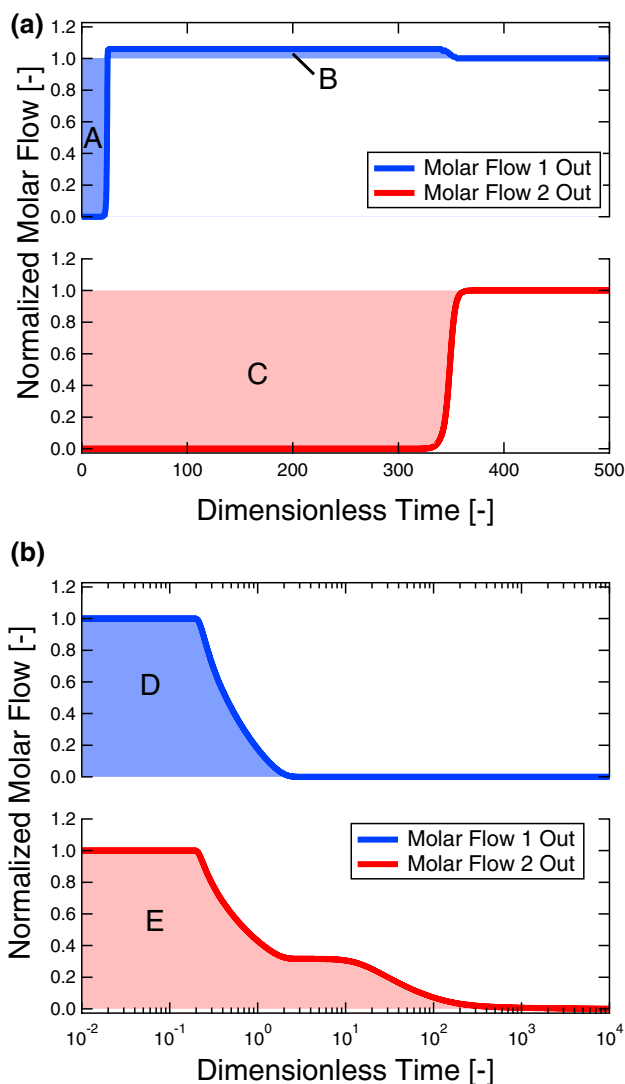


Fig. 2 A graphical representation of the solid and fluid phase accumulations for **a** adsorption and **b** desorption of a hypothetical binary mixture. The molar flows have been normalized to the component inlet flow rate so that 1 represents the component inlet flowrate. For adsorption, component 1 and 2 have an accumulation of [A – B] and C, respectively. For desorption, component 1 and 2 have an accumulation of D and E, respectively

molar flowrates for the sake of simplicity), it is important to consider the breakthrough curves for both components. As seen in Fig. 2a, for a period of time the outlet molar flow of component 1 is greater than its flowrate at the inlet. This is referred to as the “roll-up” and is crucial to determine the competitive equilibrium loading of component 1. The roll-up is the amount of component 1 that is forced out of the column due to adsorptive competition with component 2. For the desorption, the equivalent of the roll-up is now found as a plateau in the component 2 profile. Summarizing, in a binary adsorption experiment the accumulation for components 1 and 2 are the areas [A – B] and C, respectively. For the same mixture, the

desorptive accumulation for components 1 and 2 are areas D and E, respectively.

4 Experimental results

4.1 Single component equilibrium

Volumetric and gravimetric equilibrium data of CO₂ and N₂ were measured and reported in Fig. 3. The results indicate that the adsorption affinity of CO₂ is greater than N₂, with N₂ having a fairly linear isotherm, while CO₂ is nonlinear at the same temperature. Note that the data from the volumetric and gravimetric systems were consistent and can be reliably combined if there is a need to obtain data over a wide range of pressures.

The isosteric heat of adsorption, ΔH_{iso} was calculated using the Clausius-Clapeyron equation:

$$\left[\frac{\partial \ln(p_i)}{\partial (1/T)} \right]_{q_i^*} = - \frac{\Delta H_{iso}}{R} \tag{16}$$

ΔH_{iso} is related to ΔU by

$$\Delta U = \Delta H_{iso} + RT \tag{17}$$

Fig. 3c shows the calculated values ΔH_{iso} for CO₂ and N₂. These values were calculated from 25 to 100 °C and 1 mbar to 1.2 bar using the volumetric experiments. It is clear that N₂ and CO₂ show different trends as a function of loading. On the one hand, although there is a minor variation, the isosteric heat of N₂ does not change much over the loading range. This suggests that for N₂, Zeolite 13X is practically energetically homogenous (Sircar and Cao 2002; Sircar 2017). On the other hand, the isosteric heat of CO₂ decreases as the loading increases. The calculated CO₂ isosteric heats are in agreement with values found by Dirar and Loughlin (2013). At low CO₂ loadings, the isosteric heat is very high (≈ 47 kJ mol⁻¹) and low (≈ 20 kJ mol⁻¹) at high CO₂ loadings. This suggests that CO₂ adsorbs onto high energy sites at low pressures (low loadings) and once they are saturated low energy sites are occupied at high pressures (high loadings) (Sircar and Cao 2002). The ΔH_{iso} of CO₂ (in J mol⁻¹) was fit to an empirical linear equation for simulation purposes as a function of q_{CO₂} (in mol kg⁻¹):

$$\Delta H_{iso,CO_2} = -5156q_{CO_2} + 50.907 \times 10^3 \tag{18}$$

4.2 Dynamic column breakthrough experiments

4.2.1 Single component adsorption experiments

Single component CO₂ and N₂ breakthrough experiments were performed at ≈ 0.98 bar and ≈ 22 °C. A summary of the

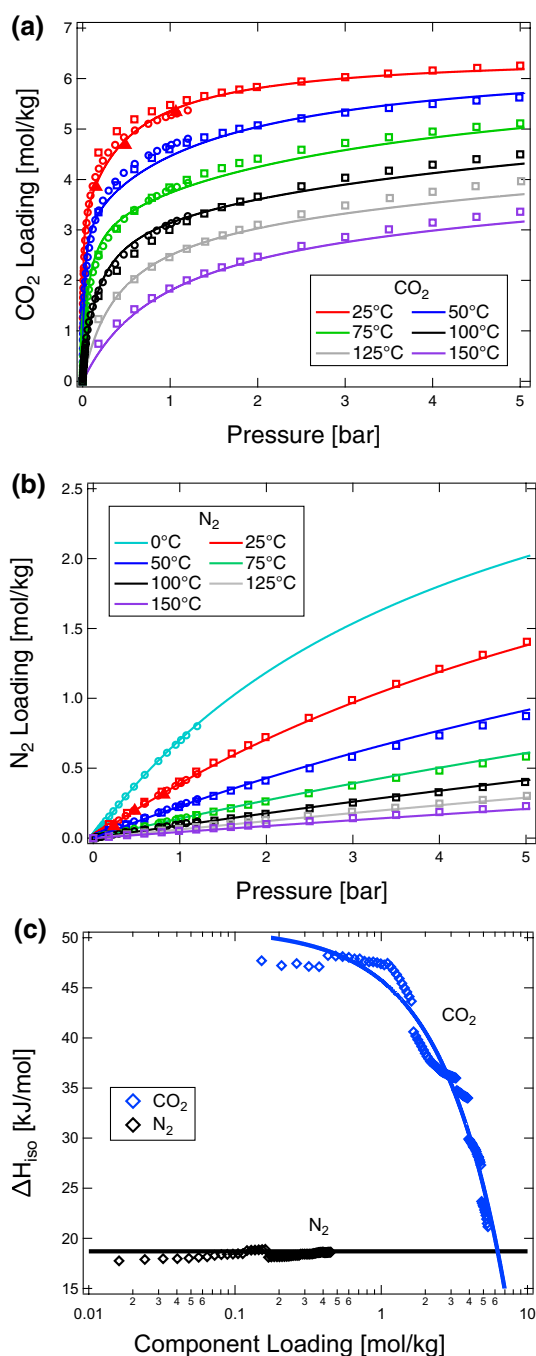


Fig. 3 Single component adsorption equilibrium on Zeolite 13X for **a** CO₂ and **b** N₂, symbols represent experimentally measured data and the lines represent isotherm fits. Volumetric data are circles, gravimetric data are squares and DCB experiments are triangles. The lines shown here for N₂ correspond to the EES model. **c** Measured (symbols) and fitted (lines) isosteric heats for CO₂ and N₂

breakthrough experiments is shown in Table 1. For all breakthrough experiments, He was used as a carrier gas. The results are reported in dimensionless time, \bar{t} , which is calculated as

$\bar{t} = tv/L$, where t is the experimental time, v is the interstitial velocity at the column inlet and L is the packed length.

The results of the single-component N₂ breakthrough experiments at 25, 50 and 85 mol% N₂ are shown in Fig. 4a. All the experimental breakthrough curves exit at $\bar{t} \approx 10$. The observation that the average retention time (corresponding to the first moment) is nearly independent of concentration indicates the linearity of the N₂ isotherm. The temperature histories show a similar trend, they all reach their peaks at about the same time. The slight difference in breakthrough times between the different feed compositions corresponds to the change in velocity associated with the adsorption of N₂ along the packed bed length. The maximum temperature reached increases with increasing N₂ feed composition. The N₂ loadings from the DCB experiments (triangles), calculated using Eq. 13, compare well with static equilibrium experiments (circles and squares) as shown in Fig. 3b and reported in Table 1.

The results of the single component CO₂ adsorption breakthrough experiments at 15, 50 and 100 mol% CO₂ are shown in Fig. 4. The composition breakthrough is shown in Fig. 4c while the temperature history is shown in Fig. 4d. As expected for Type 1 isotherms, the breakthrough time increases as the feed composition of CO₂ reduces (Mazzotti and Rajendran 2013). The composition breakthrough shows the classical shock transition starting from $y_{\text{CO}_2} = 0$. The smooth transition to the feed composition can be attributed to the non-isothermal nature of the process. The high heat of adsorption can be seen from the maximum temperatures (up to 100 °C) observed in these experiments. It is worth noting that the thermal wave propagates slower when the composition is lower; this is different than the case of N₂ where all the thermal waves propagate at approximately the same speed. Finally, the CO₂ loading was calculated from Eq. 13 and is shown in Fig. 3a as triangles. It is clear that the loadings match well with those from the batch experiments. The consistency in loadings between the three experiments (volumetry, gravimetry and DCB) confirm that the Zeolite sample is reasonably consistent and reproducible.

4.2.2 Binary adsorption experiments

After the single component breakthroughs were completed, competitive adsorption CO₂/N₂ breakthroughs were measured. Experiments were performed with CO₂/N₂ compositions of: 15/85, 50/50 and 75/25 mol% at $T = 22$ °C, $P = 0.98$ bar and $Q_{in} = 350$ ccm. A summary of all the competitive breakthrough experiments are shown in Table 1 and the adsorption breakthrough curves are shown in Fig. 5. As seen from the breakthrough curves, N₂ breaks through very early and the outlet composition of N₂ reaches 100 mol%. This classic “roll-up” effect is well known and has been reported for competitive systems obeying Type 1 isotherms.

Table 1 A summary of all adsorption and desorption experiments

Experiment type	Gas	Q_{in} (ccm)	T (°C)	P (bar)	y_{CO_2} (–)	y_{N_2} (–)	$q_{CO_2}^*$ (mol kg ⁻¹)	$q_{N_2}^*$ (mol kg ⁻¹)
Adsorption	N ₂ /He	350	22.7	0.96	–	0.25	–	8.53×10^{-2}
	N ₂ /He	351	23.0	0.96	–	0.50	–	0.195
	N ₂ /He	350	23.0	0.96	–	0.85	–	0.311
	CO ₂ /He	700	21.8	1.02	0.15	–	3.854	–
	CO ₂ /He	315	21.9	0.97	0.50	–	4.685	–
	CO ₂ /He	350	22.1	1.07	1.00	–	5.501	–
	CO ₂ /N ₂	500	23.1	1.06	0.05	0.95	2.909	[0]
	CO ₂ /N ₂	498	22.9	1.05	0.10	0.90	3.461	[0]
	CO ₂ /N ₂	300	22.0	1.02	0.15	0.85	3.833	[0]
	CO ₂ /N ₂	201	23.5	0.95	0.50	0.50	4.814	[0]
	CO ₂ /N ₂	202	21.6	0.98	0.75	0.25	5.375	[0]
	CO ₂ /N ₂ /He	400	24.4	1.04	0.05	0.45	3.090	[0]
	CO ₂ /N ₂ /He	400	23.8	1.00	0.10	0.40	3.498	[0]
	CO ₂ /N ₂ /He	400	23.9	1.03	0.25	0.25	4.200	[0]
	CO ₂ /N ₂ /He	400	23.7	1.02	0.40	0.10	4.708	[0]
Desorption	CO ₂ /N ₂	50	22.6	0.97	0.05	0.95	–	0.1445
	CO ₂ /N ₂	50	22.1	0.97	0.10	0.90	–	0.0811
	CO ₂ /N ₂	50	23.1	0.97	0.15	0.85	–	0.0801
	CO ₂ /N ₂	50	23.8	0.97	0.50	0.50	–	0.0362
	CO ₂ /N ₂	50	23.8	0.96	0.75	0.25	–	0.0200
	CO ₂ /N ₂ /He	50	24.4	0.95	0.05	0.45	–	0.0281
	CO ₂ /N ₂ /He	50	23.9	0.95	0.10	0.40	–	0.0192
	CO ₂ /N ₂ /He	50	24.6	0.96	0.25	0.25	–	0.0186
	CO ₂ /N ₂ /He	50	24.1	0.97	0.40	0.10	–	0.0082

For the adsorption experiments, the columns “gas”, y_{CO_2} and y_{N_2} refer to the feed, while for the desorption experiments they indicate the conditions at which the column was initially saturated. The value [0] means that $q_{N_2}^*$ was calculated to be negative and they are represented as 0 to provide a meaningful result. Note that $y_{CO_2} + y_{N_2} + y_{He} = 1$

The CO₂ breakthrough is similar to the single component runs. The temperature history shown in Fig. 5c shows the presence of a small peak at very low values of \bar{t} which corresponds to the heat generated by N₂ adsorption. The temperature rise due to CO₂ adsorption is more prominent. Note that the experiments were run for a prolonged period of time until the temperature front fully broke through and the column was returned to the surrounding temperature. This is essential to perform the transient mass balance to measure the competitive loadings.

The competitive loadings of CO₂ and N₂ were calculated from the adsorption breakthrough profiles using Eq. 13. The competitive CO₂ loadings were measured with high reliability and are reported in Fig. 6 and Table 1. However, the N₂ equilibrium loadings could not be accurately calculated from the competitive breakthrough experiments. The N₂ loadings calculated with this method yielded negative values, which are physically unrealistic. Some of the experiments were repeated to check for reproducibility. Although the breakthrough curves showed excellent reproducibility,

the unrealistic N₂ loadings persisted. Similar results have been reported in the literature (Avijegon et al. 2018). This was partially due to the sensitivities and accuracies for the mass flow controllers (± 2 sccm), mass flow meter (± 1 sccm) and primary flow calibrator (± 2 ccm). However, the largest uncertainty was the accumulated error that is associated with the relatively long breakthrough time of CO₂ ($\bar{t} > 120$) to the fast N₂ breakthrough time ($\bar{t} = 10$). This uncertainty accumulates for the entire experimental time, from $\bar{t} = 10$ to at least $\bar{t} = 120$. Due to these problems, the integration of Eq. 13 often yielded unrealistic negative N₂ loadings. Figure 2a shows a qualitative picture of Eq. 13. As discussed earlier, for the case of CO₂ the shaded region **C** represents the amount of CO₂ present in the column, while for N₂ this amount of is given by $[A - B]$. As it can be seen in Fig. 2a, the areas **A** and **B** can be very similar and since the compositions and flows are measured with a finite accuracy, the calculated N₂ loadings are rather unreliable. This could possibly explain why Avijegon et al. measured negligible (≈ 0) loadings for the competitive adsorption of N₂ in mixtures of

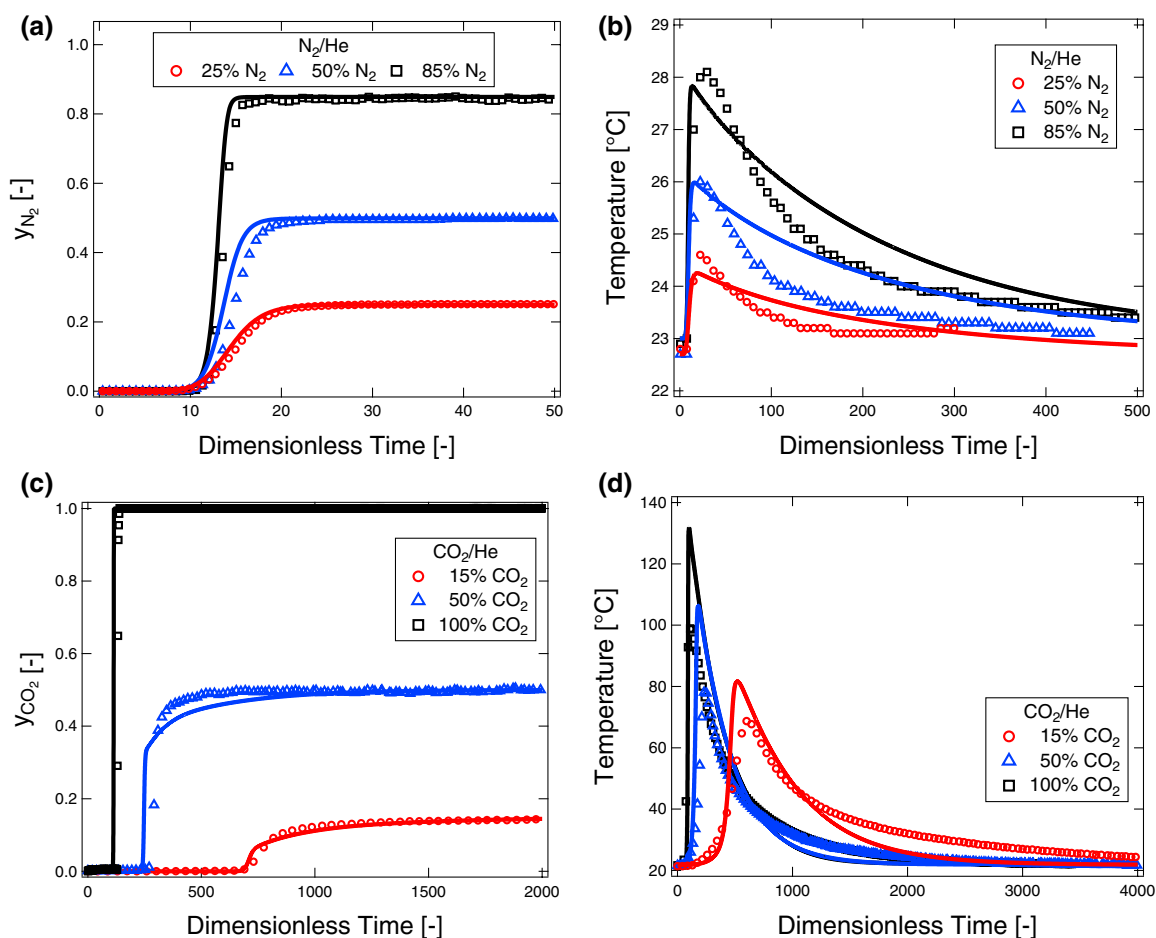


Fig. 4 Single component N_2 (a and b) and CO_2 (c and d) composition and temperature breakthrough curves on Zeolite 13X at $\approx 22^\circ C$. The carrier gas for all cases was He. Experiments are the symbols and

lines are from simulations using the EES model. The temperature is measured at $z = 0.8L$

CO_2 and N_2 at ≈ 1 bar (Avijegon et al. 2018). This analysis suggests that adsorption breakthrough experiments could result in unreliable measurements for the lighter component, when the competition between the two species is very strong. Note that such issues are not faced when gases of comparable affinities were used as seen from our previous studies with O_2 and Ar on Ag-ETS-10 where the selectivity is 1.5 (Hosseinzadeh Hejazi et al. 2016).

4.2.3 Binary desorption experiments

The adsorption breakthrough experiments provided inconclusive data for competitive N_2 adsorption. Therefore, it was decided to consider desorption experiments. The hypothesis was that in the desorption experiments, the area proportional to the accumulated amount corresponds to D in Fig. 2b, which is obtained in a short time that prevents the accumulation of error. It should be noted that for a system where the competitive loading is small, then

it is likely that the desorption is over in a very short time. Hence, in order to overcome this, we also decided to perform the desorption experiments at much lower flows. The experiments were done by first performing a breakthrough experiment with a given mixture of CO_2 , N_2 and He. After the breakthrough was complete, the adsorbing gas was switched to 50 ccm of He. Two types of experiments were performed. The first set of experiments involved saturating the bed with different compositions of CO_2 and N_2 , and desorbing it with He. In the second set of experiments, the column was saturated with a mixture of He, CO_2 and N_2 , and later desorbed with He. Various experiments were performed by fixing the He composition at 50 mol% while changing the relative proportion of CO_2 and N_2 . Since He can be considered a non-adsorbing gas, these experiments allowed us to explore competition at lower concentrations ($P = 0.48$ bar).

The details of the experiments are provided in Table 1. The competitive desorption composition and temperature profiles

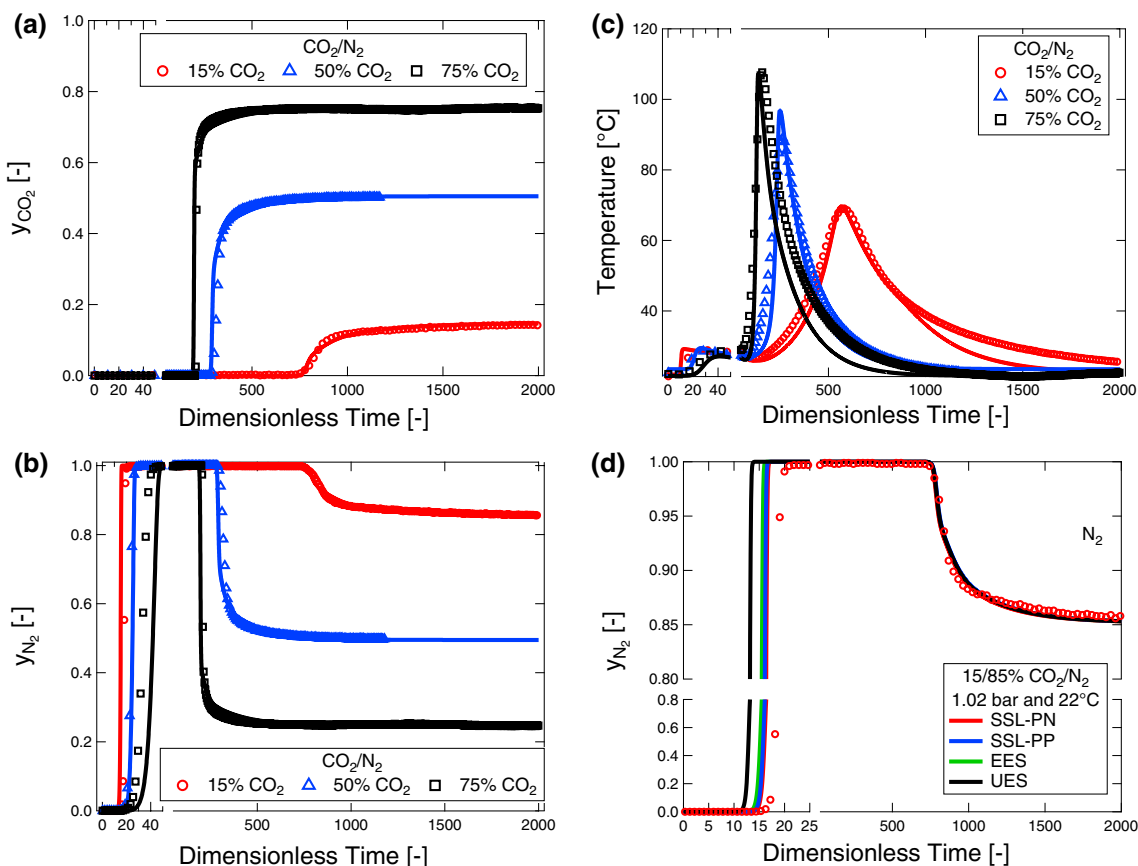


Fig. 5 Competitive (a) CO₂ and (b) N₂ composition and (c) temperature breakthrough profiles on Zeolite 13X. The competitive CO₂/N₂ breakthrough experiments are at 15/85, 50/50 and 25/75 mol% mixtures of CO₂ and N₂. Symbols are the experimental measurements

and lines are the simulations from UES parameters. **d** Comparison of the calculations by the different fitting procedures with the experimental breakthrough curve for N₂

for the case where a mixture of CO₂, N₂ and He were saturated at the beginning of the experiment are shown in Fig. 7. Similar plots for the case where the column was saturated with mixtures of CO₂ and N₂ are provided in the supporting information. As seen from Fig. 7, N₂ desorbs very quickly compared to CO₂. In this case the qualitative desorption profiles are shown in Fig. 2b. Since the experiment was performed at low flows, it resulted in a reliable estimation of the N₂ competitive loading that are plotted in Fig. 6. Owing to the strong CO₂ isotherm, the desorption can take an unusually long time and the experiments were not extended beyond $\bar{t} \approx 500$. Accordingly, competitive CO₂ loadings were not measured from the desorption experiments. In order to calculate the competitive N₂ loading, Eq. 15 was integrated between $\bar{t} = 0$ and 500. The measured competitive N₂ loadings are shown in Fig. 6. It can be seen that these experiments provided physically realistic, meaningful, N₂ loadings compared to the adsorption breakthrough experiments. It is also worth noting that the N₂ loadings obtained from the desorption experiments compare well with those reported by Hefti et al. (2015).

5 Parameter estimation and modeling results

5.1 Isotherm parameter estimation

Several isotherm models have been proposed in the literature to describe the equilibrium of CO₂ and N₂ on Zeolite 13X. The goal in this study is to consider forms that are easy to describe and have a straightforward, explicit extension to competitive forms so that they can be used for large-scale simulation and optimization. Recently, Purdue has discussed the use of a dual-site model to describe CO₂ isotherms to reliably represent CO₂ adsorption on Zeolite 13X (Purdue 2018). The variation of the isosteric heat with loading lends itself to support this argument; that CO₂ adsorbs to a heterogeneous surface. Further, Farmahini et al. also demonstrated the ability of the dual-site Langmuir (DSL) model to describe single component isotherms of CO₂ and N₂ (Farmahini et al. 2018). The DSL model for a binary mixture is expressed as:

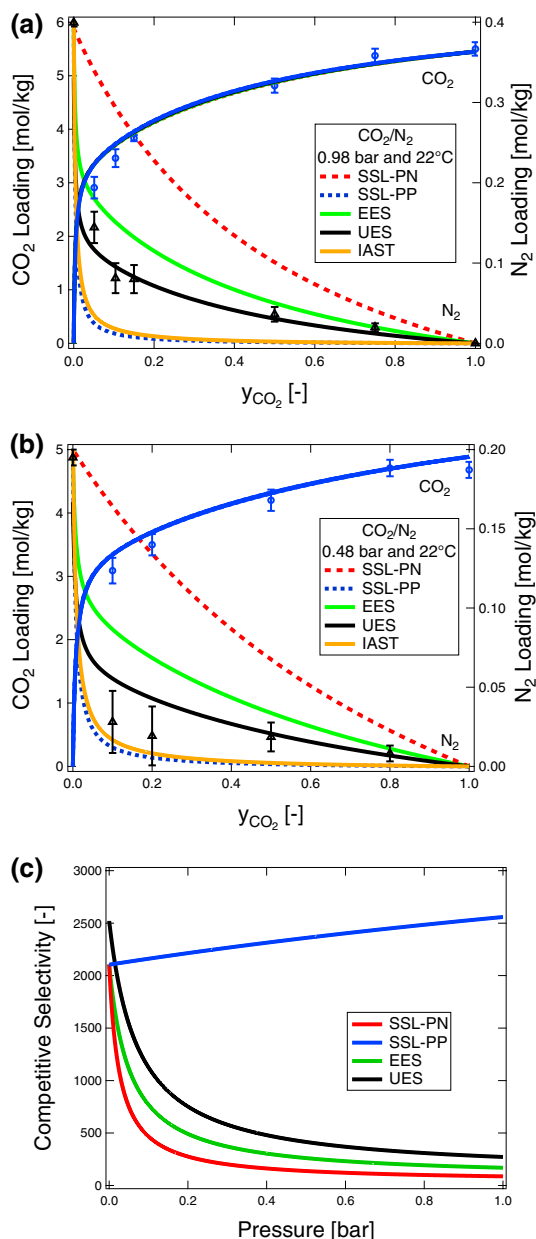


Fig. 6 Competitive CO₂ (circles) and N₂ (triangles) equilibrium loadings from DCB and desorption experiments on Zeolite 13X at a total pressure of 0.98 (a) and 0.48 (b) bar at 22 °C. CO₂ is shown in blue and N₂ is shown in black. The different equilibrium fitting procedures are shown with IAST predictions. (c) Calculated competitive CO₂/N₂ selectivities for a 15/85 mol% mixture as a function of total pressure at 25 °C. The error bars show the 95% confidence intervals of each measurement. (Color figure online)

$$q_i^* = \frac{q_{b,i}^{\text{sat}} b_i c_i}{1 + b_1 c_1 + b_2 c_2} + \frac{q_{d,i}^{\text{sat}} d_i c_i}{1 + d_1 c_1 + d_2 c_2} \quad (19)$$

where q_b^{sat} and q_d^{sat} are the saturation capacities of the two sites b and d , respectively. The equilibrium constants b_i and d_i are dependent on temperature as described by:

$$b_i = b_{0,i} \exp\left(\frac{-\Delta U_{b,i}}{RT}\right) \quad (20)$$

$$d_i = d_{0,i} \exp\left(\frac{-\Delta U_{d,i}}{RT}\right) \quad (21)$$

$\Delta U_{b,i}$ and $\Delta U_{d,i}$ are the internal energies of adsorption to sites b and d , respectively. The sites “ b ” and “ d ” represent the strong and the weak sites, respectively.

Determining the correct isotherm parameters is critical. Several ways have been proposed to estimate the parameters. Farmahini et al. recently discussed a few ways of fitting the CO₂ and N₂ isotherms (Farmahini et al. 2018). In their study three methods were proposed. The first two involved fitting CO₂ isotherms first, then setting the saturation capacity of N₂ for both sites to be identical to that of CO₂ and then fitting the b and d constants to different constraints. The third involved a more detailed fit considering the Henry’s constant of both components and low temperature isotherms. In the current work we adapt an approach similar to Farmahini et al. First the DSL model is fitted to the experimentally measured CO₂ isotherms. The parameters, namely $q_{b,\text{CO}_2}^{\text{sat}}$, $q_{d,\text{CO}_2}^{\text{sat}}$, b_{0,CO_2} , d_{0,CO_2} , $\Delta U_{b,\text{CO}_2}$ and $\Delta U_{d,\text{CO}_2}$, were fitted simultaneously using the data points between 0 and 1.2 bar for the temperatures 25–100 °C. The goal was to obtain an accurate fit for the range of pressures where the model will be used. The parameters are listed in Table 2. As can be seen, the ΔU values, for the two sites corresponds approximately to the upper and lower bounds of the ΔH_{iso} shown in Fig. 3c (note the relationship between ΔH_{iso} and ΔU is given by Eq. 17). Four different procedures were used to estimate the parameters for the N₂ isotherm:

Single site Langmuir (SSL): The single site Langmuir isotherm fitting procedure(SSL) is the first approach. The SSL uses a single site Langmuir isotherm by forcing $q_{\text{N}_2}^{\text{sat}} = q_{b,\text{CO}_2}^{\text{sat}} + q_{d,\text{CO}_2}^{\text{sat}}$ and then fitting b_{0,N_2} and $\Delta U_{b,\text{N}_2}$ to the experimental data. Variations of this approach have been used in the literature (Xiao et al. 2008; Krishnamurthy et al. 2014a). The implicit assumption here is that the adsorbent is homogeneous with respect to N₂. The volumetric single-component data between $P = 0\text{--}1.2$ bar and $T = 25\text{--}100$ °C were used for the fitting procedure. Parameters obtained by this fitting method are shown in Table 2. Note that the ΔU obtained nicely corresponds to the ΔH_{iso} shown in Fig. 3c. Since the DSL model was used to describe the CO₂ isotherms, there are two possible ways to combine the SSL parameters for N₂ to describe the competitive behavior. The SSL perfect positive (SSL-PP) fitting procedure refers to the case where the SSL parameters are paired with the b site of the CO₂ and for the SSL perfect negative (SSL-PN), the SSL parameters of N₂ are paired with the d site (Ritter et al. 2011). Note that the values of equilibrium constants and ΔU for the two approaches are,

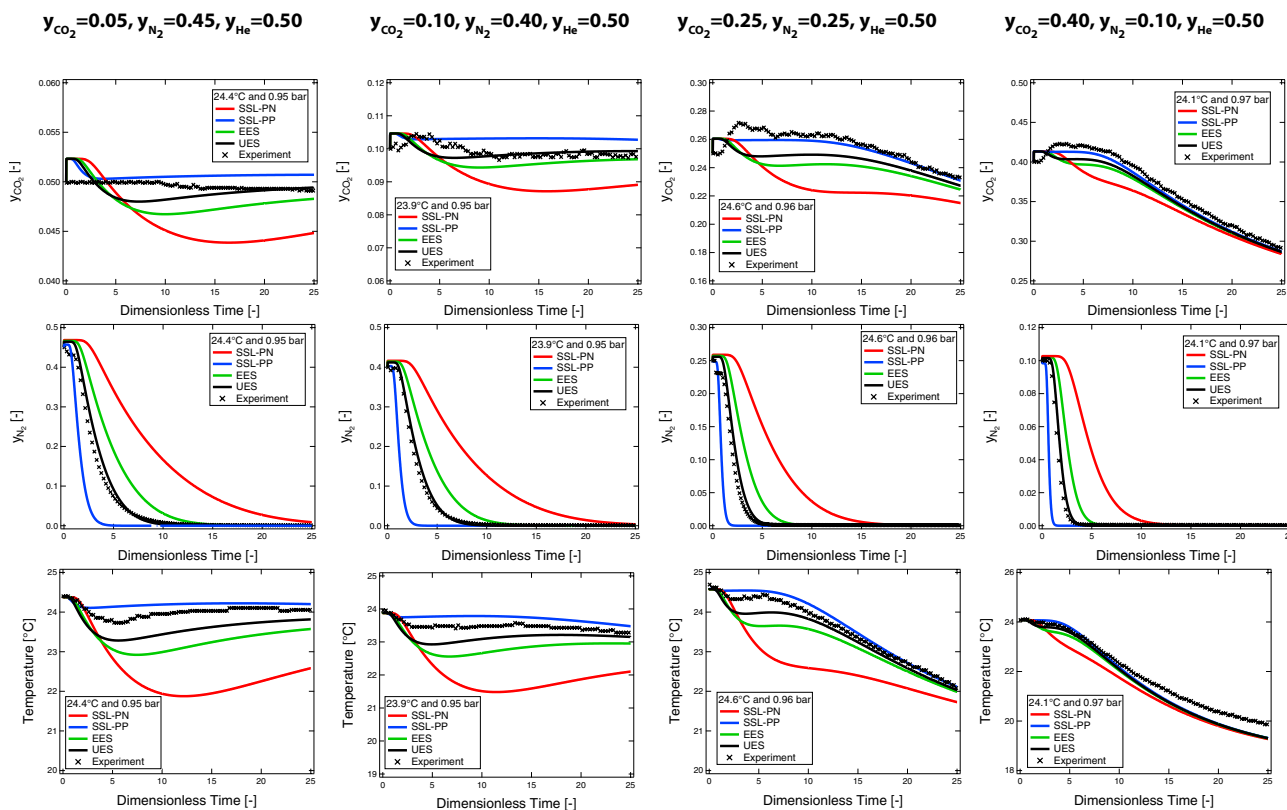


Fig. 7 Competitive CO₂/N₂ composition (top and middle row) and temperature (bottom row) desorption profiles on Zeolite 13X at ≈ 22 °C and 0.48 bar. Experiments are the markers and simulations are the various lines. These experiments were diluted with 50 mol% He

as expected, the same. What changes is just the pairing with the CO₂ isotherm.

Dual site Langmuir with equal energy sites (EES): In this case N₂ is considered to be distributed between two equal energy sites (hence EES) with the saturation capacity of each site identical to that of CO₂ (Farmahini et al. 2018). In other words, the following conditions are enforced:

$$q_{b,N_2}^{sat} = q_{b,CO_2}^{sat} \tag{22}$$

$$q_{d,N_2}^{sat} = q_{d,CO_2}^{sat} \tag{23}$$

$$b_{0,N_2} = d_{0,N_2} \tag{24}$$

$$\Delta U_{b,N_2} = \Delta U_{d,N_2} \tag{25}$$

Note that while Eqs. 22 and 23 are required to obtain the thermodynamically consistent form of a DSL isotherm (Myers 1983; Farmahini et al. 2018), Eqs. 24 and 25 enforce a condition that N₂ sees a homogenous surface. Variations of this approach have been used in the literature (Farmahini et al. 2018; Nikolaidis et al. 2018). The

during adsorption. The initial compositions are provided at the top of each column of figures. Temperature is measured at $z = 0.8L$. Desorption was performed using a sweep of He at 50 ccm

volumetric single-component data between $P = 0–1.2$ bar and $T = 25–100$ °C were used for the fitting procedure and the parameters are provided in in Table 2.

Dual site Langmuir with unequal energy sites (UES): In this case the restriction of equal energy sites (Eqs. 24 and 25) is removed. The sorbent is considered to possess unequal energy sites (UES) also for N₂. Only the constraints described in Eqs. 22 and 23 are enforced. For this case, the competitive N₂ loadings were also considered to fit the model. In other words the objective function that is used to fit the parameters now includes both the data from the volumetric experiments and the binary data from the breakthrough experiments. Naturally, the relaxation of the equal energy requirements and the use of the binary data should provide this approach an advantage over the others. The fitting parameters are shown in Table 2. As it can be seen the estimated values of ΔU_b and ΔU_d vary by ≈ 6%, indicating that the model recognizes that the two sites are of comparable energy. While this fitting procedure provides a better estimate of the binary data, it underpredicts the single-component data up to ≈ 15%. This compromise was necessary to in order to fit the binary data in an explicit form.

IAST: Ideal adsorbed solution theory (IAST) was used as a comparison for these models. IAST was developed by Myers and Prausnitz to describe ideal adsorption competition on an adsorbent (Myers and Prausnitz 1965). This approach provides a method to calculate competitive loadings based on single-component isotherms. The method to calculate the competitive loadings using the IAST is provided in the supporting information.

5.1.1 Comparison of isotherm parameter estimation approaches

Figure 6 shows the calculated competitive loadings of CO₂ and N₂ as a function of CO₂ composition at a total pressure of 0.98 and 0.48 bar at 22 °C. It can be seen that the competitive CO₂ loadings are essentially unaffected by the type of competitive isotherm chosen. However, the N₂ loading is significantly impacted by the competitive model. The SSL-PP model, where N₂ competes with the strong site of CO₂, predicts the lowest N₂ loading, while the SSL-PN, where N₂ competes with the weak site of CO₂, predicts the highest N₂ loading. The EES and UES fitting procedures predict intermediate N₂ loadings. The EES predicts a slightly higher loading compared to the UES fitting procedure. IAST for all N₂ isotherms predicts competition very close to the SSL-PP fitting procedure. It is important to note that the IAST calculations under-predict the observations by Hefti et al. (2015).

The competitive selectivity, $\alpha_{\text{CO}_2, \text{N}_2}$, for a mixture is calculated using:

$$\alpha_{\text{CO}_2, \text{N}_2} = \frac{q_{\text{CO}_2}^*(y_{\text{CO}_2}) y_{\text{N}_2}}{q_{\text{N}_2}^*(y_{\text{N}_2}) y_{\text{CO}_2}} \quad (26)$$

The competitive selectivities were determined as a function of total pressure for all four fitting procedures for a mixture of 15/85 mol% CO₂/N₂, i.e., corresponding to a typical feed composition of a post-combustion CO₂ capture plant, and are shown in Fig 6 c. The selectivities of SSL-PN, EES and UES follow the expected trend, i.e., where α decreases as the pressure increases. Specifically, in this case, the selectivity drops from ≈ 2000 – 2500 to 100 – 300 . The selectivities calculated by the the three procedures decrease in the following order UES > EES > SSL-PN. However, the SSL-PP fitting procedure provides a physically unrealistic picture where α increases with pressure. This is due to the weak adsorption of N₂ in the SSL-PP fitting procedure, which affects the high-energy sites that get filled at low pressures. At high pressures, the low energy sites start to dominate and there is virtually no competition from N₂ on these sites. Hence, at higher pressures the SSL-PP likely will overpredict the performance of Zeolite 13X

5.2 Dynamic column breakthrough simulations

5.2.1 Parameter estimation

Parameters for the experiments and simulations are provided in Table 3. The bulk density of the adsorbent, ρ_{bulk} , was measured by weighing a volume of adsorbent from a graduated cylinder after the particles had been well packed. The bulk void fraction, ϵ , was calculated from the particle size and column diameter (De Klerk 2003). The particle void fraction, ϵ_p , the specific heat capacity of the adsorbent, $C_{p,s}$, the specific heat capacity of the column wall, $C_{p,w}$, the thermal conductivity of the wall, K_w , the column density, ρ_w and the tortuosity, τ , were assumed to be the same as in Haghpanah et al. (2013a), which used a similar Zeolite 13X sample and a stainless steel column. The specific heat capacity of the gas mixtures, $C_{p,g}$ were taken as standard values for each different gas mixture; these values were obtained using the NIST REFPROP v9.1 database (Lemmon et al. 2013). The specific heat capacity of the adsorbed phase, $C_{p,a}$, was assumed to be the same as $C_{p,g}$ since no information was known about $C_{p,a}$. The molecular diffusion, D_m , for all mixtures was found using the Chapman–Enskog equation (Wankat 2007). The internal and external heat transfer coefficients, h_{in} and h_{out} , and the effective gas thermal conductivity, K_z , were determined via an optimization to match the thermal breakthrough profiles of the single component CO₂ DCB experiments; this procedure was done to ensure the thermal breakthrough profiles were matched since N₂ releases less energy during adsorption.

5.2.2 Single component adsorption experiments

After the experimental DCB adsorption and desorption experiments were performed and quantified, they were simulated using the different fitting procedures. For all of the adsorption experiments, the EES fitting procedure is shown as the simulation unless otherwise specified. The single component CO₂ and N₂ DCB adsorption experiments are shown in Fig. 4. From Fig. 4b, the temperature profiles are matched reasonably, but the temperature decay after the adsorptive heat front passed the thermocouple is faster in the experiment than in the simulation; overall, the temperature difference between the experiment and the simulation is within 1 °C. For the CO₂ experiments, the comparison of the simulated and experimental temperature histories is good. The CO₂ breakthrough experiments were at two different flowrates. The 15% CO₂ experiments were carried out at 700 ccm while the 50 and 100 mol% CO₂ experiments were at 315 and 350 ccm, respectively. This was due to limitations of the flow controllers utilized in the breakthrough apparatus. The value of h_{in} reported in Table 3 was determined by an optimization to fit all of the

CO₂ experiments. The composition breakthrough simulations agree with the experiments for both CO₂ and N₂.

5.2.3 Binary adsorption experiments

Figure 5 shows that the simulated breakthrough curves for CO₂ predict the experimental measurements well. This is highlighted in Fig. 5d, where all four fitting procedures are shown for the 15/85 mol% experiment. IAST was not simulated since the computation effort is large and it is very similar to the SSL-PP fitting procedure. In the case of N₂, for the duration of the entire experiment, all the fitting procedures seem to predict the curves very well. Upon zooming into the earlier breakthrough, all four methods predict an earlier breakthrough, with the UES predicting a much earlier breakthrough compared to the others. Further, focussing on the end of the roll-up, it is practically impossible to differentiate between the different calculations. From a simulation perspective, it is challenging to identify which of the isotherm fitting procedure should be selected for N₂ just from the binary adsorption experiments.

5.2.4 Binary desorption experiments

The desorption curves were simulated for the various fitting procedures and the profiles are shown in Fig. 7 (see supporting information for more comparisons). The comparisons of the N₂ desorption breakthrough and the prediction of the temperature profiles together shows clearly the distinction between the various fitting procedures. The SSL-PP (blue lines) predicts the least amount of N₂ loading and therefore leaves the column very quickly. This is reflected in the temperature profiles with essentially no change in temperature during the N₂ desorption. The SSL-PN (red lines) predicts the greatest competitive N₂ loading and takes the longest to desorb N₂. In this case, the largest change in temperature for N₂ desorption is seen. The EES (green lines) fitting procedure provides a good predictive description of the CO₂/N₂ competition; these predictions fall between the SSL-PP and SSL-PN fitting procedures. The UES (black lines) clearly shows an excellent prediction of the curves for the cases of N₂, CO₂ and temperature, especially the excellent match of the CO₂ composition profiles. Here again, the UES fitting procedure shows a better prediction compared to the other fitting procedures.

6 Effect of isotherm parameters on process performance

In the previous sections the importance of describing the CO₂/N₂ competition was elaborated. It is important to understand the impact of these descriptions on the process

performance. For this we consider a 4-step VSA cycle with light product pressurization (LPP), a VSA configuration that has been used extensively to compare post-combustion CO₂ capture adsorbents (Haghpanah et al. 2013; Krishnamurthy et al. 2014b; Rajagopalan et al. 2016).

The 4-step VSA cycle configuration studied is shown in Fig. 8. It consists of an adsorption step, a co-current blowdown, an counter-current evacuation and finally a LPP using part of the collected raffinate from the ADS step (Haghpanah et al. 2013b). A description of the cycle steps is found below.

Adsorption (ADS): Feed gas enters the column at $z = 0$ at a given T and P_H . The heavy product (CO₂) adsorbs into the adsorbent, while the light product (N₂) leaves the $z = L$ end of the column.

Blowdown (BLO): The feed end of the column ($z = 0$) is closed and a vacuum is pulled from the raffinate end of the column ($z = L$). The pressure changes from P_H to an intermediate pressure, P_I , in this step. This removes most of the N₂ within the column, increasing the concentration of CO₂.

Evacuation (EVAC): The raffinate end of the column ($z = L$) is closed and the feed end ($z = 0$) is opened and a

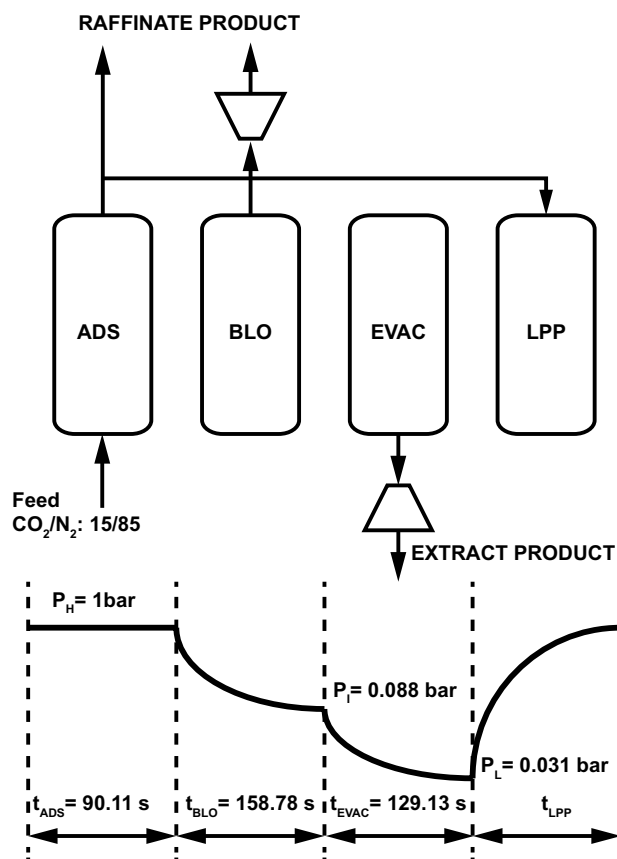


Fig. 8 The schematic of the 4-step cycle with LPP. The values of the various operating parameters used for the study is also shown

deeper vacuum is pulled. The pressure changes from P_1 to the lowest pressure in the cycle, P_L . This step concentrates CO_2 at the feed end and collects it as the heavy product.

Light product pressurization (LPP): This step takes part of the light product from the adsorption step and reintroduces it to the column in a reverse pressurization from $z = L$ while the feed end of the column ($z = 0$) is closed. This enriches the raffinate end of the column with N_2 and sharpens the CO_2 front, and forces CO_2 towards the feed end of the column.

The key process performance indicators are defined as follows

$$\text{Purity, } Pu = \frac{n_{\text{CO}_2, \text{EVAC}}}{n_{\text{CO}_2, \text{EVAC}} + n_{\text{N}_2, \text{EVAC}}} \quad (27)$$

$$\text{Recovery, } Re = \frac{n_{\text{CO}_2, \text{EVAC}}}{n_{\text{CO}_2, \text{ADS}}} \quad (28)$$

$$\text{Energy, } En = \frac{E_{\text{ADS}} + E_{\text{BLO}} + E_{\text{EVAC}}}{n_{\text{CO}_2, \text{EVAC}}} \quad (29)$$

where each of E_{ADS} , E_{BLO} and E_{EVAC} are calculated using

$$E = \frac{1}{\eta} \frac{\gamma}{\gamma - 1} \int_{t=0}^{t=t_{\text{step}}} QP \left[\left(\frac{1}{P} \right)^{\frac{\gamma-1}{\gamma}} - 1 \right] dt \quad (30)$$

where $\eta = 0.72$ is the efficiency of the vacuum pump and γ is the ratio of the heat capacities.

To determine the effect of N_2 on process performance, a set of process conditions were used to simulate the SSL-PP, SSL-PN, EES and UES fitting procedures in the 4-step LPP cycle for a 15/85 mol% CO_2/N_2 feed at 25 °C and 1 bar. The parameters were taken from Rajagopalan et al. and are $t_{\text{ADS}} = 90.11$ s, $t_{\text{BLO}} = 158.78$ s, $t_{\text{EVAC}} = 129.13$ s, $P_1 = 0.088$ bar, $P_L = 0.031$ bar and $v_{\text{in}} = 0.37$ m/s. The column and adsorbent parameters were taken from Haghpanah et al. (2013a) and are shown in the supporting information. For each case, the column was considered to be initially saturated with N_2 at 1 bar pressure. The single column switches from one step to the others in a periodic fashion. The LPP step is implemented by storing the output of the adsorption step in a data buffer and using it to pressurize the column. The blowdown step removes the N_2 to purify the bed, while the evacuation recovers the CO_2 from the bed. This was continued until the process reached cyclic steady state.

The impact of the fitting procedures for describing the N_2 isotherm is shown in Fig. 9. The purity/recovery values shown in Fig. 9a indicate that as the competitive loading of N_2 increases in the order SSL-PP, UES, EES, SSL-PN (from left to right in Fig. 9), the CO_2 purity decreases, while its recovery increases. The change is small for both purity and

recovery (< 2%) between the SSL-PP, UES and EES fitting procedures, but significantly larger for the SSL-PN fitting procedure ($\approx 6.5\%$). Figure 9b shows that an increase in $q_{\text{N}_2}^*$ increases the parasitic energy. The change between the DSL fitting procedures is significantly larger for the energy predictions; when compared to UES fitting procedure the change is between 9 and 40%. Figure 9b also shows how much energy is used in each of the constituent steps. The parasitic energy in the adsorption step is marginal and stays relatively the same. The evacuation energy requirement marginally increases with the increase in $q_{\text{N}_2}^*$, but practically remains the same. However, the amount of energy required for the blowdown step increases significantly with $q_{\text{N}_2}^*$. This is the step in the VSA process where the majority of the N_2 is removed. The SSL-PP and EES fitting procedures require $\approx 43\%$ less and more energy than the UES fitting procedure respectively, while the SSL-PN process requires $\approx 166\%$ more blowdown energy compared to UES.

To understand how the predicted $q_{\text{N}_2}^*$ can change the process performance, it helps to look at the amount of moles removed for the adsorption, blowdown and evacuation constituent steps in Figs. 9c and d. The total moles of CO_2 , n_{CO_2} , and N_2 , n_{N_2} , removed remains constant at irrespective of the four DSL fitting procedures as the operating conditions have been kept the same. However, the amount of CO_2 and N_2 removed in each step changes depending on how much N_2 adsorbs. The majority of CO_2 is removed in the evacuation step. This amount becomes slightly larger as the predicted $q_{\text{N}_2}^*$ increases. The amount of CO_2 removed in the blowdown also slightly increases with $q_{\text{N}_2}^*$. Finally, the amount of CO_2 lost in the desorption step decreases with increasing $q_{\text{N}_2}^*$. The overall change for each constituent step is not very large for the SSL-PP, UES and EES fitting procedures, but the change for the SSL-PN fitting procedure is very significant. This increased amount of CO_2 recovered in the evacuation and decreased amount of CO_2 lost in the adsorption step improves the recovery of the process as the predicted $q_{\text{N}_2}^*$ increases. For N_2 , shown in Fig. 9d, the change between the fitting procedures is very apparent. As the predicted $q_{\text{N}_2}^*$ increases, the amount of N_2 removed increases in the blowdown and evacuation steps, while decreasing in the adsorption step. This shows that as $q_{\text{N}_2}^*$ increases, more N_2 is collected with the CO_2 product in the evacuation step, reducing the product purity. Also the separation between CO_2 and N_2 becomes more difficult since, less N_2 is collected in the adsorption step. This helps explain why the predicted energy requirement is greater at a higher predicted $q_{\text{N}_2}^*$; more energy must be spent to remove the excess amount of N_2 trapped within the adsorbent in the blowdown and evacuation steps.

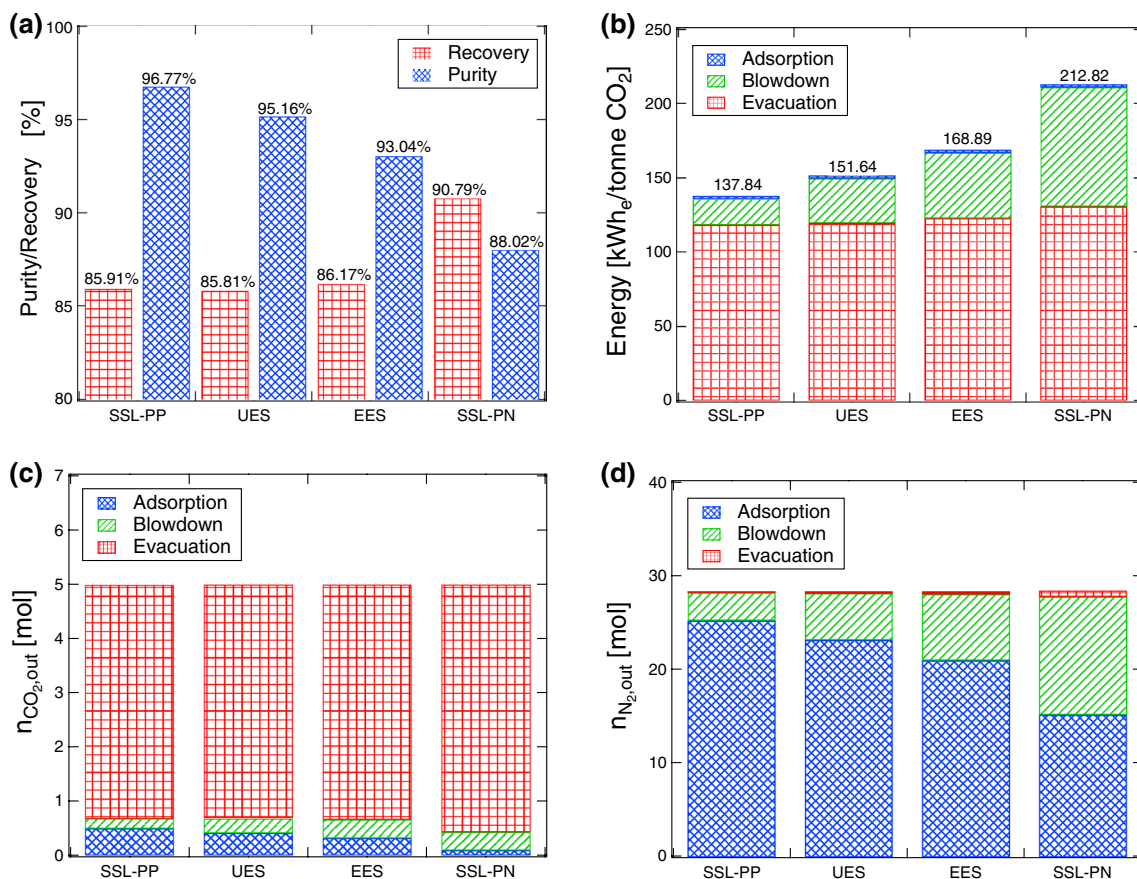


Fig. 9 Impact of the fitting procedure on the process performance predictions. The bar graphs are ordered from the smallest to largest predicted $q_{N_2}^*$. The **a** purities and recoveries, **b** the breakdown of the energy consumption of each step and the moles of **c** CO₂ and **d** N₂

collected per cycle for all the fitting procedures for the 4-step LPP cycle performed at, $t_{ADS} = 90.11$ s, $t_{BLO} = 158.78$ s, $t_{EVAC} = 129.13$ s, $P_I = 0.088$ bar, $P_L = 0.031$ bar and $v = 0.37$ m/s

Table 2 DSL isotherm parameters for pure components on Zeolite 13X

Gas	Model	q_b^{sat} (mol kg ⁻¹)	b_0 (m ³ mol ⁻¹)	$-\Delta U_b$ (kJ mol ⁻¹)	q_d^{sat} (mol kg ⁻¹)	d_0 (m ³ mol ⁻¹)	$-\Delta U_d$ (kJ mol ⁻¹)
CO ₂	DSL	3.257	2.09×10^{-7}	42.67	3.240	1.06×10^{-7}	32.21
N ₂	SSL	6.497	2.15×10^{-6}	16.23	0	0	0
N ₂	EES	3.257	2.13×10^{-6}	16.25	3.240	2.13×10^{-6}	16.25
N ₂	UES	3.257	7.96×10^{-7}	18.86	3.240	6.94×10^{-7}	17.76

7 Conclusions

CO₂ and N₂ competition on Zeolite 13X was studied. Isotherms for CO₂ and N₂ were measured using volumetry and gravimetry at 0 (only N₂), 25, 50, 75, 100, 125 and 150 °C between 1 mbar and 5 bar. Adsorption equilibrium data was fit to a DSL isotherm for both CO₂ and N₂. N₂ was fit to a series of DSL isotherm isotherms that describe CO₂/N₂ competition differently. These fitting procedures all make different assumptions of the N₂ adsorption sites and how

CO₂ competes with those adsorption sites. It was found that while the UES fitting procedure was able to describe the binary equilibrium data most accurately, it underpredicted the single component loading of N₂. However, if binary data is not collected the EES fitting procedure provides a decent predictive description of the binary CO₂/N₂ competition. Pure DCB experiments for CO₂ and N₂ were performed at ≈ 0.98 bar and 22 °C. Helium was used as a carrier for all breakthrough experiments. All DCB adsorption experiments were modeled and simulated using the EES isotherm in the adsorption simulator. The DCB experiments and simulations

Table 3 Adsorption and desorption simulation parameters for Zeolite 13X

	Value	Source
Column properties		
Adsorbent mass, m_{ads} (g)	23.02	Measured
Column length, L (m)	6.4×10^{-2}	Measured
Inner column diameter, d_i (m)	2.82×10^{-2}	Manufacturer
Outer column diameter, d_o (m)	3.18×10^{-2}	Measured
Column void fraction, ϵ	0.4	Assumed
Particle void fraction, ϵ_p	0.35	Assumed
Tortuosity, τ	3	Assumed
Properties and constants		
Universal gas constant, R ($\text{m}^3 \text{Pa mol}^{-1} \text{K}^{-1}$)	8.314	Standard value
Adsorbent particle density, ρ_p (kg m^{-3})	961.7	Assumed
Column wall density, ρ_w (kg m^{-3})	7800	Standard value
Specific heat capacity of the gas, $C_{p,g}$ ($\text{J mol}^{-1} \text{K}^{-1}$)	1600 (N_2/He) 1440 (CO_2/He) 922 (CO_2/N_2)	NIST database
Specific heat capacity of the adsorbed phase, $C_{p,a}$ ($\text{J mol}^{-1} \text{K}^{-1}$)	$C_{p,g}$	Assumed
Specific heat capacity of the adsorbent, $C_{p,s}$ ($\text{J mol}^{-1} \text{K}^{-1}$)	856	Assumed
Specific heat capacity of the column wall, $C_{p,w}$ ($\text{J mol}^{-1} \text{K}^{-1}$)	502.0	Standard value
Fluid viscosity, μ ($\text{kg m}^{-1} \text{s}^{-1}$)	1.812×10^{-5}	Standard value
Molecular diffusion, D_m ($\text{m}^2 \text{s}^{-2}$)	1.6×10^{-5}	Chapman–Enskog
Effective gas thermal conductivity, K_z ($\text{W m}^{-1} \text{K}^{-1}$)	0.19	Fitted
Thermal conductivity of column wall, K_w ($\text{W m}^{-1} \text{K}^{-1}$)	16.0	Standard value
Internal heat transfer coefficient, h_{in} ($\text{W m}^{-2} \text{K}^{-1}$)	11.0	Fitted
External heat transfer coefficient, h_{out} ($\text{W m}^{-2} \text{K}^{-1}$)	10.0	Fitted

displayed good agreement between both composition and temperature breakthrough profiles. After pure components were simulated, competitive CO_2/N_2 breakthrough experiments were measured at ≈ 0.98 bar and 22°C and simulated with the adsorption simulator. All binary experiments matched the simulated breakthrough predictions for all DSL fitting procedures well. However, it was not possible to determine which fitting procedure was the most accurate using the DCB profiles, since all fitting procedures predicted very similar composition and thermal breakthrough profiles. The competitive N_2 loadings were not able to be quantified with any certainty due to experimental limitations and the inherently low loading of N_2 in competitive CO_2/N_2 mixtures. Therefore, competitive desorption experiments were performed to obtain a clear distinction between the equilibrium models. The competitive desorption experiments were at $\approx 22^\circ\text{C}$, 0.98 and 0.48 bar and with a 50 ccm inlet flow of He. The N_2 loading could be quantified from the competitive desorption experiments with certainty. The binary CO_2/N_2 equilibrium could then be quantified fully; CO_2 was measured using competitive DCB experiments and N_2 from the competitive desorption experiments. A process study under dry conditions with a fixed set of operating conditions (at 25°C and 1 bar) showed that the purity, recovery and parasitic energy depended on the predicted competitive

N_2 loading. The purity and recovery percent deviation from the unequal energy site fitting procedure was between 2–8% and 0.1–6%, respectively. The parasitic energy deviated up to 40% from the UES fitting procedure. The main conclusion of this study is that competitive CO_2/N_2 equilibrium data must be collected to accurately understand VSA process performance. Using single component CO_2 and N_2 isotherms for predictive competitive models can only give an approximation of the process performance.

Acknowledgements Funding support from the Canada Foundation for Innovation Project Number 33801 and Canada First Excellence Fund through University of Alberta Future Energy Systems are acknowledged. We thank Zeochem for providing samples of the Zeolite 13X used in this study.

References

- Avijegon, G., Xiao, G., Li, G., May, E.F.: Binary and ternary adsorption equilibria for $\text{CO}_2/\text{CH}_4/\text{N}_2$ mixtures on zeolite 13X beads from 273 to 333 K and pressures to 900 kPa. *Adsorption* **24**(4), 381–392 (2018)
- Boot-Handford, M.E., Abanades, J.C., Anthony, E.J., Blunt, M.J., Brandani, S., Dowell, N Mac, Fernández, J.R., Ferrari, M., Gross, R., Hallett, J.P.: Carbon capture and storage update. *Energy Environ. Sci.* **7**(1), 130–189 (2014)

- Bui, M., Adjiman, C.S., Bardow, A., Anthony, E.J., Boston, A., Brown, S., Fennell, P.S., Fuss, S., Galindo, A., Hackett, L.A.: Carbon capture and storage (CCS): the way forward. *Energy Environm. Sci.* **11**(5), 1062–1176 (2018)
- Cavenati, S., Grande, C.A., Rodrigues, A.E.: Separation of CH₄/CO₂/N₂ mixtures by layered pressure swing adsorption for upgrade of natural gas. *Chem. Eng. Sci.* **61**(12), 3893–3906 (2006)
- De Klerk, A.: Voidage variation in packed beds at small column to particle diameter ratio. *AIChE J.* **49**(8), 2022–2029 (2003)
- Dirar, Q.H., Loughlin, K.F.: Intrinsic adsorption properties of CO₂ on 5A and 13X zeolite. *Adsorption* **19**(6), 1149–1163 (2013)
- Farmahini, A.H., Krishnamurthy, S., Friedrich, D., Brandani, S., Sarkisov, L.: From crystal to adsorption column: challenges in multi-scale computational screening of materials for adsorption separation processes. *Ind. Eng. Chem. Res.* **57**, 15491–15511 (2018)
- Gleuckauf, E., Coates, J.I.: The influence of incomplete equilibrium on the front boundary of chromatograms and the effectiveness of separation. *J. Chem. Soc.* **1315**, e21 (1947)
- Guntuka, S., Farooq, S., Rajendran, A.: A-and B-site substituted lanthanum cobaltite perovskite as high temperature oxygen sorbent. 2. Column dynamics study. *Ind. Eng. Chem. Res.* **47**(1), 163–170 (2008)
- Haghpanah, R., Majumder, A., Nilam, R., Rajendran, A., Farooq, S., Karimi, I.A., Amanullah, M.: Multiobjective optimization of a four-step adsorption process for postcombustion CO₂ capture via finite volume simulation. *Ind. Eng. Chem. Res.* **52**(11), 4249–4265 (2013a)
- Haghpanah, R., Nilam, R., Rajendran, A., Farooq, S., Karimi, I.A.: Cycle synthesis and optimization of a VSA process for postcombustion CO₂ capture. *AIChE J.* **59**(12), 4735–4748 (2013b)
- Hefiti, M., Marx, D., Joss, L., Mazzotti, M.: Adsorption equilibrium of binary mixtures of carbon dioxide and nitrogen on zeolites ZSM-5 and 13X. *Microporous Mesoporous Mater.* **215**, 215–228 (2015)
- Hocker, T., Rajendran, A., Mazzotti, M.: Measuring and modeling supercritical adsorption in porous solids. carbon dioxide on 13X zeolite and on silica gel. *Langmuir* **19**(4), 1254–1267 (2003)
- Hosseinzadeh Hejazi, S.A., Rajendran, A., Sawada, J.A., Kuznicki, S.M.: Dynamic column breakthrough and process studies of high-purity oxygen production using silver-exchanged titanasilicates. *Ind. Eng. Chem. Res.* **55**(20), 5993–6005 (2016)
- Hu, X., Mangano, E., Friedrich, D., Ahn, H., Brandani, S.: Diffusion mechanism of CO₂ in 13X zeolite beads. *Adsorption* **20**(1), 121–135 (2014)
- IPCC: Special report on carbon capture and storage. Technical report, Intergovernmental Panel on Climate Change (IPCC) (2005)
- Krishnamurthy, S., Haghpanah, R., Rajendran, A., Farooq, S.: Simulation and optimization of a dual-adsorbent, two-bed vacuum swing adsorption process for CO₂ capture from wet flue gas. *Ind. Eng. Chem. Res.* **53**(37), 14462–14473 (2014a)
- Krishnamurthy, S., Rao, V.R., Guntuka, S., Sharratt, P., Haghpanah, R., Rajendran, A., Amanullah, M., Karimi, I.A., Farooq, S.: CO₂ capture from dry flue gas by vacuum swing adsorption: a pilot plant study. *AIChE J.* **60**(5), 1830–1842 (2014b)
- Lemmon, E.W., Huber, M.L., McLinden, M.O.: NIST standard reference database 23: reference fluid thermodynamic and transport properties-REFPROP, version 9.1. NIST Pubs (2013)
- Lu, W., Ying, Y., Shen, W., Li, P., Yu, J.: CO₂ capture from flue gas in an existing coal power plant. In *6th Pacific Basin Conference on Adsorption Science and Technology, Taipei, May*, pp. 20–23 (2012)
- Mazzotti, M., Rajendran, A.: Equilibrium theory-based analysis of non-linear waves in separation processes. *Annu. Rev. Chem. Biomol. Eng.* **4**, 119–141 (2013)
- Myers, A.L.: Activity coefficients of mixtures adsorbed on heterogeneous surfaces. *AIChE J.* **29**(4), 691–693 (1983)
- Myers, A.L., Prausnitz, J.M.: Thermodynamics of mixed-gas adsorption. *AIChE J.* **11**(1), 121–127 (1965)
- Nikolaidis, G.N., Kikkinides, E.S., Georgiadis, M.C.: A model-based approach for the evaluation of new zeolite 13X-based adsorbents for the efficient post-combustion CO₂ capture using P/VSA processes. *Chem. Eng. Res. Des.* **131**, 362–374 (2018)
- Purdue, M.J.: Explicit flue gas adsorption isotherm model for zeolite 13X incorporating enhancement of nitrogen loading by adsorbed carbon dioxide and multi-site affinity shielding of co-adsorbate dependent upon water vapor content. *J. Phys. Chem. C* **122**, 11832–11847 (2018)
- Rajagopalan, A.K., Rajendran, A.: The effect of nitrogen adsorption on vacuum swing adsorption based post-combustion CO₂ capture. *Int. J. Greenh. Gas Control* **78**, 437–447 (2018)
- Rajagopalan, A.K., Avila, A.M., Rajendran, A.: Do adsorbent screening metrics predict process performance? A process optimisation based study for post-combustion capture of CO₂. *Int. J. Greenh. Gas Control* **46**, 76–85 (2016)
- Rajendran, A., Hocker, T., Di Giovanni, O., Mazzotti, M.: Experimental observation of critical depletion: nitrous oxide adsorption on silica gel. *Langmuir* **18**(25), 9726–9734 (2002)
- Rajendran, A., Kariwala, V., Farooq, S.: Correction procedures for extra-column effects in dynamic column breakthrough experiments. *Chem. Eng. Sci.* **63**(10), 2696–2706 (2008)
- Ritter, J.A., Bhadra, S.J., Ebner, A.D.: On the use of the dual-process Langmuir model for correlating unary equilibria and predicting mixed-gas adsorption equilibria. *Langmuir* **27**(8), 4700–4712 (2011)
- Ruthven, D.M.: Principles of Adsorption and Adsorption Processes. Wiley, Hoboken (1984)
- Samanta, A., Zhao, A., Shimizu, G.K.H., Sarkar, P., Gupta, R.: Post-combustion CO₂ capture using solid sorbents: a review. *Ind. Eng. Chem. Res.* **51**(4), 1438–1463 (2011)
- Sircar, S.: Gibbsian surface excess for gas adsorption revisited. *Ind. Eng. Chem. Res.* **38**(10), 3670–3682 (1999)
- Sircar, S.: Basic research needs for design of adsorptive gas separation processes. *Ind. Eng. Chem. Res.* **45**(16), 5435–5448 (2006)
- Sircar, S.: Comments on practical use of Langmuir gas adsorption isotherm model. *Adsorption* **23**(1), 121–130 (2017)
- Sircar, S., Cao, D.V.: Heat of adsorption. *Chem. Eng. Technol.* **25**(10), 945–948 (2002)
- Smit, B., Reimer, J.A., Oldenburg, C.M., Bourg, I.C.: Introduction to Carbon Capture and Sequestration. World Scientific, Singapore (2014)
- Stern, N.: The economics of climate change. *Am. Econ. Rev.* **98**(2), 1–37 (2008)
- Wang, Y., LeVan, M.D.: Adsorption equilibrium of carbon dioxide and water vapor on zeolites 5A and 13X and silica gel: pure components. *J. Chem. Eng. Data* **54**(10), 2839–2844 (2009)
- Wankat, P.C.: Separation Process Engineering. Prentice Hall, Upper Saddle River (2007)
- Xiao, P., Zhang, J., Webley, P., Li, G., Singh, R., Todd, R.: Capture of CO₂ from flue gas streams with zeolite 13X by vacuum-pressure swing adsorption. *Adsorption* **14**(4–5), 575–582 (2008)
- Zanco, S.E., Joss, L., Hefiti, M., Gazzani, M., Mazzotti, M.: Addressing the criticalities for the deployment of adsorption-based CO₂ capture processes. *Energy Proced.* **114**, 2497–2505 (2017)